Numerical analysis of hydroelasticity problems by coupling WCSPH with multibody dynamics

Ada Yilmaz [*], Selahattin Kocaman , Mustafa Demirci

Iskenderun Technical University, Department of Civil Engineering, 31200, Iskenderun, Hatay, Turkey

A B S T R A C T

This paper aims to extend the implementation of DualSPHysics-Project Chrono coupling to hydroelasticity problems involving free-surface flows and deformable elastic boundaries. In the present model, the fluid sub-domain of the phenomenon is based on the WCSPH model of DualSPHysics. The solid sub-domain, simulated by the Project Chrono engine, is modeled using the set of rigid bodies attached by hinges with torsional and damping stiffness. An analytical solution of Euler-Bernoulli beam theory is employed to adapt the rigid-multibody system to the mechanical characteristics of the elastic sub-domain via the torsional stiffness values of hinges. The stability and accuracy of the present model are tested by three cases with different flow characteristics and mechanical properties for solid sub-domain, involving a newly-designed experimental setup and two benchmark cases in the literature. Obtained results show reasonable accuracy with experimental measurements and other numerical model computations.

1. Introduction

In the context of the Fluid-Structure Interaction (FSI) problems, the hydroelasticity phenomenon is encountered frequently in ocean engineering field. Typical examples are wave/tsunami surge impact on offshore/coastal structures, sloshing in LNG tanks, and hydrodynamic slamming on ships and ocean structures (Khayyer et al., 2019, 2021). The phenomenon with violent free-surface flows and deformable boundaries is too complex to solve using analytical methods due to the nature of the problem with multi-physics and nonlinearity (Wu et al., 2016). Therefore, numerical and experimental studies have become the main tools for researchers in the investigation of the phenomenon. In addition, with the rapid developments in computational technology and some limitations in experimental studies, there is a growing importance of numerical models.

The mesh-free numerical methods present a quite convenient structure for numerical modeling of hydroelasticity problems. Thanks to meshless Lagrangian natures, these methods can easily handle large deformations and moving interfaces avoiding difficulties encountered in conventional mesh-based methods (Bašić et al., 2020; Sun et al., 2019). One of the most popular of these methods, Smoothed Particle Hydrodynamics (SPH) was firstly introduced in astrophysics (Gingold and Monaghan, 1977; Lucy, 1977) and later successfully applied to various

free-surface flow problems (Altomare et al., 2017; Areu-Rangel et al., 2021; Colicchio et al., 2002; Crespo et al., 2008; Han and Dong, 2020; Iglesias et al., 2004; Monaghan, 1994; Xu et al., 2021). With the success of the method in numerical modeling of free-surface flows, various forms of SPH have started to be used in hydroelasticity analyses by many researchers (e.g. Weakly Compressible SPH (WCSPH)-SPH (Antoci et al., 2007; Liu et al., 2013), WCSPH-Total Lagrangian SPH (TLSPH) (Han and Hu, 2018; He et al., 2017; O'Connor and Rogers, 2021; Sun et al., 2021; Zhan et al., 2019), and Incompressible SPH (ISPH)-SPH (Khayyer et al., 2018, 2021; Rafiee and Thiagarajan, 2009)).

Considering the capability of SPH to overcome the numerical difficulties faced in hydroelasticity problems, some researchers have tried to take advantage of the method via coupling with other numerical frameworks (e.g. Finite Element Method (Groeneboom and Cartwright, 2010; Li et al., 2015; Panciroli et al., 2012; Yang et al., 2012; Yilmaz et al., 2021), Discrete Element Method (Tang et al., 2018; Wu et al., 2016), and Element Bending Group (Yang et al., 2016)). The numerical implementation of multibody solver Project Chrono (Tasora and Anitescu, 2011) under the SPH model of DualSPHysics (Crespo et al., 2015; Domínguez et al., 2021) makes it possible to simulate the interaction between free-surface flows and rigid body systems with collisions and kinematic restrictions such as springs, hinges, and pulleys. Canelas et al. (2018) applied this coupling procedure to various fluid-mechanism

---

* Corresponding author.
  E-mail address: ada.yilmaz@iste.edu.tr (A. Yilmaz).

interaction problems. Some researchers used DualSPHysics-Project Chrono coupling to simulate the motion of oscillating wave surge converters (OWSC) involving a rigid flap attached to the ground with a bottom hinge with mechanical constraints (Brito et al., 2016, 2020; Liu et al., 2020). Ropero-Giralda et al. (2020) employed this coupling procedure to simulate a point-absorber wave energy converter system composed of a rigid buoy connected to a PTO system modeled as a linear damper. Also, Wei et al. (2019) simulated the interaction of WECs with water waves by coupling Project Chrono with another SPH solver, GPUSPH. To the authors' best knowledge, despite a lot of studies on various fluid-mechanism interaction problems, the present coupling scheme is not implemented comprehensively to hydroelasticity problems.

This paper aims to extend the implementation of DualSPHysics-Project Chrono coupling to hydroelasticity problems involving violent free-surface flows and deformable elastic boundaries. In the present numerical model, the solid phase of the phenomenon is modeled using a rigid-multibody system attached by hinges with torsional and damping stiffness. While the DualSPHysics code is employed to solve fluid sub-domain and fluid-rigid body interactions, the Project Chrono library is employed to solve the mechanical constraints between rigid bodies. The rigid-multibody system is adopted to the mechanical characteristics of elastic sub-domain by torsional stiffness values of hinges calculated by an analytical solution of Euler-Bernoulli beam theory. The stability and accuracy of the present model are investigated by using a new experimental study of dam-break wave impact on an elastic baffle in a wet bed and experimental and numerical results of two benchmark cases in the literature.

The rest of the paper is organized as follows; numerical backgrounds of the WCSPH model in DualSPHysics, multibody solver of Project Chrono, and coupling procedure of these two models are explained in Section 2. Section 3 presents an analytical solution of Euler-Bernoulli beam theory to calculate the torsional stiffness values of hinges. Then, the solution accuracy of the present numerical model is tested in Section 4 using a newly-designed experimental setup and two benchmark cases. Finally, the conclusion is drawn in Section 5.

2. Numerical model

2.1. SPH model of DualSPHysics

DualSPHysics (Crespo et al., 2015) is an open-source code based on the WCSPH formulation of SPH. This code is implemented in C++ and Compute Unified Device Architecture (CUDA), allowing to run simulations with multiple Central Processing Units (CPU) or Graphics Processing Units (GPU) (Brito et al., 2020; Domínguez et al., 2013).

In SPH, the conservation laws of continuum fluid dynamics are transformed from their partial differential form using integral equations based on an interpolation function called kernel *(W)*. A function *F(r)* can be written by the mentioned integral approximation as;

$$F(\boldsymbol{r}) = \int F(\boldsymbol{r}') \, W(\boldsymbol{r} - \boldsymbol{r}', h) d\boldsymbol{r}'. \tag{1}$$

where *r* is the position vector and *h* is the smoothing length defining the support region of the kernel. Eq. (1) can be written in discrete notation, leading to an approximation of function at a particle *a*, where the summation is over all the particles *b* within the support region of the kernel function;

$$F(\boldsymbol{r}_a) \approx \sum_b F(\boldsymbol{r}_b) \frac{m_b}{\rho_b} \, W(\boldsymbol{r}_a - \boldsymbol{r}_b, h). \tag{2}$$

where ρ and m are the density and mass of the particles, respectively. The performance of an SPH model depends heavily on the choice of the smoothing kernel (Crespo et al., 2015). In this work, the fifth-order Quintic kernel (Wendland, 1995) is used, considering its higher order

of interpolation (Gomez-Gesteira et al., 2010) and benefits in the free-surface flow simulations (Macia et al., 2011);

$$W(r, h) = a_D \left(1 - \frac{q}{2}\right)^4 (2q + 1) \quad 0 \le q \le 2 \tag{3}$$

where q is the non-dimensional distance between the particles, which is $q = r/h$, and r is the distance between the particles a and b. a_D is equal to $7/4\pi h^2$ and $21/16\pi h^3$ for 2D and 3D problems, respectively. The kernel function provides a compact support region of *2h* radius, in which neighboring particles are considered ($q \le 2$).

2.1.1. Equations of motion

The governing equations of motion are described by the Navier–Stokes equations for compressible fluids (Domínguez et al., 2021). The mass and momentum conservation equations can be written in the discrete form of SPH as follows, respectively;

$$\frac{D\rho_a}{Dt} = \rho_a \sum_b \frac{m_b}{\rho_b} (\boldsymbol{v}_a - \boldsymbol{v}_b) \cdot \nabla_a W_{ab} + \delta_\varphi h c_0 \sum_b \frac{m_b}{\rho_b} \Psi_{ab} \cdot \nabla_a W_{ab} \tag{4}$$

$$\frac{D\boldsymbol{v}_a}{Dt} = -\sum_b m_b \left(\frac{P_b + P_a}{\rho_b \rho_a} + \Pi_{ab}\right) \nabla_a W_{ab} + \boldsymbol{g} \tag{5}$$

where $\boldsymbol{v}$ is the velocity, t is the time, P is the pressure and $\boldsymbol{g}$ is the gravitational acceleration. In the continuity equation, the second term on the right-hand side represents the numerical density diffusion term used to reduce fluctuation in density and consequently pressure. Ψ_{ab} is the density diffusion function introduced by Molteni and Colagrossi (2009) and modified later by Fourtakas et al. (2019). δ_φ is the constant that controls the intensity of the diffusive term. In momentum equation, Π is the artificial viscosity term proposed by Monaghan (1992);

$$\Pi_{ab} = \begin{cases} \frac{-\alpha \overline{c_{ab}} \mu_{ab}}{\overline{\rho_{ab}}} & (\boldsymbol{v}_a - \boldsymbol{v}_b) \cdot (\boldsymbol{r}_a - \boldsymbol{r}_b) < 0 \\ 0 & (\boldsymbol{v}_a - \boldsymbol{v}_b) \cdot (\boldsymbol{r}_a - \boldsymbol{r}_b) > 0 \end{cases} \tag{6}$$

where $\overline{c_{ab}} = 0.5(c_a + c_b)$ is the mean speed of sound, $\mu_{ab} = h(\boldsymbol{v}_a - \boldsymbol{v}_b)\$(\boldsymbol{r}_a - \boldsymbol{r}_b)/((\boldsymbol{r}_a - \boldsymbol{r}_b)^2 + 0.01h^2)$ and, α is the artificial viscosity constant, introducing the proper energy dissipation.

In WCSPH formulation, the fluid is treated as weakly compressible and the following equation of state is used to determine fluid pressure based on particle density (Batchelor, 1974; Monaghan et al., 1999);

$$P = B \left[\left(\frac{\rho}{\rho_0}\right)^\gamma - 1 \right] \tag{7}$$

where ρ_0 is the reference density of the fluid, $\gamma = 7$, and $B = c_0^2 \rho_0 / \gamma$ where c_0 is the speed of sound at the reference density.

In this work, Verlet (1967) algorithm is used for the time integration scheme and, a variable time step proposed by Monaghan and Kos (1999) is considered, based on the force per unit mass, viscous diffusion term, and Courant-Friedrich-Levy (CFL) condition with a *CFL* number of 0.2.

2.1.2. Boundary conditions

The Dynamic Boundary Condition (DBC) (Crespo et al., 2007) available in DualSPHysics is implemented in the present SPH model. In this method, the boundary particles are seen same as the fluid particles and satisfy the same equations. But, they do not move by the forces exerted and remain either fixed in position or move according to an imposed/assigned motion function. When a fluid particle enters inside the neighboring list of the boundary particles, defined by the smoothing length *(h)*, the density of that boundary particles increases, resulting in a pressure increase. This situation causes a repulsive force to be exerted on the fluid particle due to the pressure term in the momentum equation. The DBC provides computational simplicity since the boundary particles are calculated inside the same loops as fluid ones and, the stability of this

method relies on the length of time step (Crespo et al., 2015).

2.1.3. Motion of rigid bodies

In SPH, rigid bodies consist of sets of discrete particles whose variables are integrated in time with a different set of equations (Canelas et al., 2015). The net force on each boundary particle k is calculated as the sum of the contributions of all surrounding particle a;

$$f_k = \frac{dv_k}{dt} = \sum_{a \in WPs} \frac{dv_{ka}}{dt} \tag{8}$$

The basic equations of the motion of the rigid body are;

$$M\frac{dV}{dt} = \sum_{k \in boundary} m_k f_k \tag{9}$$

$$I\frac{d\Omega}{dt} = \sum_{k \in boundary} m_k (r_k - R_0) \times f_k \tag{10}$$

where M is the mass of the object, I moment of inertia, V the velocity and Ω the rotational velocity and R_0 center of mass. Eqs. (9) and (10) can be integrated in time to predict the values of V and Ω at the beginning of the next time step and each boundary particle of the rigid body has a velocity;

$$v_k = V + \Omega \times (r_k - R_0) \tag{11}$$

All the boundary particles within the rigid body are moved by integrating Eq. (11) in time. The works of Monaghan (2005) and Monaghan et al. (2003) showed that the technique conserves both linear and angular momentum.

2.2. Project Chrono

The rigid multibody systems are described in Project Chrono by a generalized coordinate system q, which have six independent coordinates $q = [R^T, \Theta^T]^T$, where R and Θ are the translational and rotational coordinates, respectively. Once this set of coordinates is identified, the global position of an arbitrary point on the body can be expressed in terms of q and the dynamic of rigid bodies can be characterized by differential-algebraic equations (Tasora et al., 2016);

$$\frac{dq}{dt} = L(q)V \tag{12}$$

$$M(q)\frac{dV}{dt} = F_a(V, q, t) + \sum_{i=1}^{p} (\gamma_{i,n} D_{i,n} + \gamma_{i,u} D_{i,u} + \gamma_{i,w} D_{i,w}) \tag{13}$$

where L is the Jacobian matrix connecting V to the derivative of q, M is the inertia matrix, and F_a is the applied force. $\gamma_{i,n}$, $\gamma_{i,u}$ and $\gamma_{i,w}$ are the Lagrange multiplier and $D_{i,n}$, $D_{i,u}$ and $D_{i,w}$ are the tangent space generators, where n, u, and w are the orientation of local reference frames at contact point i, where n is the normal and u and w are the tangential component (Mazhar et al., 2015). In the present numerical model, the contacts between the solid bodies are neglected and Project Chrono is used to simulate the hinges with torsional and damping stiffness, connecting the rigid bodies, composed the solid phase of the phenomenon. The mathematical formulation, describing the dynamic equilibrium of the hinges with a single degree of freedom, can be written as (Brito et al., 2016);

$$I\frac{d\Omega}{dt} = \tau - K_\Theta \Theta - K_\Omega \Omega \tag{14}$$

where τ is the external torque, Θ is the rotation angle, Ω is the angular velocity, and K_Θ and K_Ω are the torsional and damping stiffness coefficients of hinges, respectively.

2.3. Coupling of DualSPHysics and Project Chrono

The coupling procedure of DualSPHysics-Project Chrono consists of three main steps (Brito et al., 2020). At first, DualSPHysics computes the motion of fluid particles by solving Eqs. (4) and (5). The interaction between fluid and rigid body particles is computed by an application of the Dynamic Boundary Condition (Canelas et al., 2015, 2018). In this approach, the fluid particles see the rigid-body particles as the regular boundary particles. But, the force from fluid particles contributes to the acceleration of the rigid-body particles (Eq. (8)), resulting in a motion governed by Eqs. (9) and (10). In the second step, linear and angular acceleration vectors *(dV/dt and dΩ/dt)* are transferred to the Chrono engine to be applied to the center of mass of the rigid bodies. Project Chrono updates rigid body motions considering the kinematic restrictions using Eqs. (12)–(14) and, the value of R_0, V, and Ω are transferred back to DualSPHysics code. Finally, DualSPHysics updates the position of the particles using Eq. (11). The flow chart of the related coupling procedure is presented in Fig. 1.

3. Calculation of torsional stiffness values for hinges (K_Θ)

In this work, a pseudo-rigid-body model (Howell, 2001) is used to approximate the deformation characteristics of solid sub-domains in the present hydroelasticity problems. With this model, the deflection of a flexible solid sub-domain is tried to predict accurately using rigid-body components attached by torsion springs. The pseudo-rigid-body model (PRBM) requires less computational cost. However, approximation accuracy depends on rigid-body configurations and, PRBM can be designed for the cases in which the type of expected load and boundary conditions are known. Many researchers successfully implemented the PRBM in modeling large-deflection beams in various rigid-body configurations (Howell and Midha, 1994; Su, 2009; Venkiteswaran and Su, 2015; Yu and Zhu, 2017).

In PRBM, the force-deflection relationship of a beam is determined by the stiffness values of springs named hinges in this work. These values depend on the mechanical properties and boundary conditions of beams used in analyses. In all validation cases used in this work, solid plates are located as one side fixed and another side free (Fig. 2). Therefore, related torsional stiffness values can be calculated using the kinematic and static equations obtained from an analytical solution of a cantilever beam under uniformly distributed loads. In this regard, deflections at tip points of each rigid-body *(w(x))* are calculated firstly using Euler-Bernoulli beam theory as follows;

$$w(x) = \frac{qx^2(6L^2 - 4Lx + x^2)}{24EI} \tag{15}$$

where q is the uniformly distributed load, E is Young's modulus, I is the second moment of area, and L is the length of the beam.

Then, calculated deflections are used to approximate rotation angles of hinges by using the equation below;

$$\Theta_i = \sin^{-1}\left(\frac{w_{i+1} - w_i}{l}\right) \tag{16}$$

where Θ_i is the rotation angle of the hinge, and l is the length of each rigid body. The relative rotation angles for each hinge can be calculated by;

$$\Delta\Theta_i = \Theta_i - \Theta_{i-1} \tag{17}$$

Finally, torsional stiffness values of hinges ($K_{\Theta i}$) can be calculated using the equation below;

$$K_{\Theta i} = \frac{\tau_i}{\Delta\Theta_i} \tag{18}$$

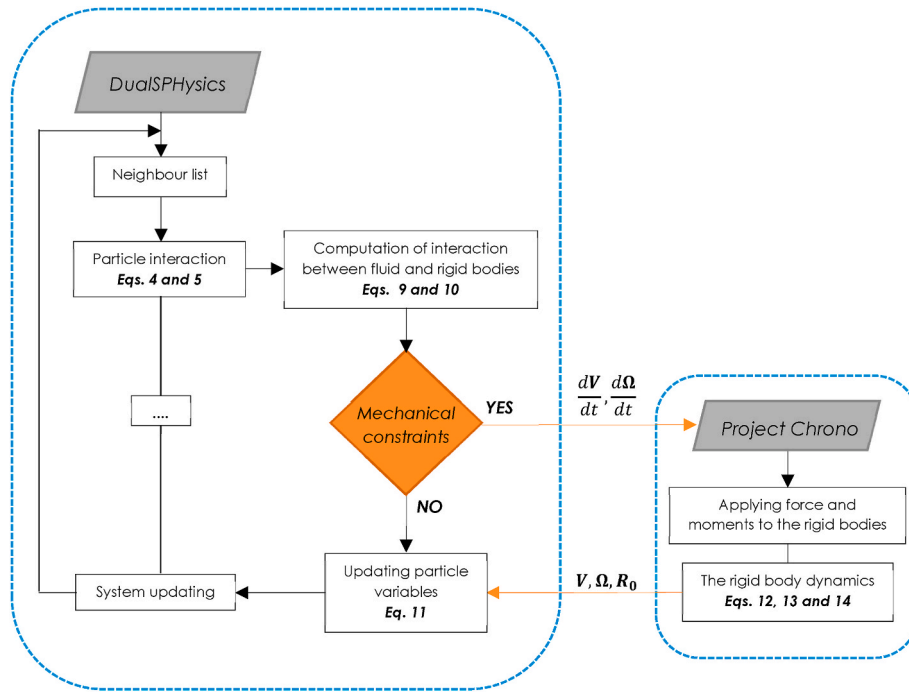where τ_i is the torque at specific hinge locations, calculated by static equations.

Fig. 1. Flow chart of the coupling procedure of DualSPHysics and Project Chrono (modified from Brito et al. (2020)).
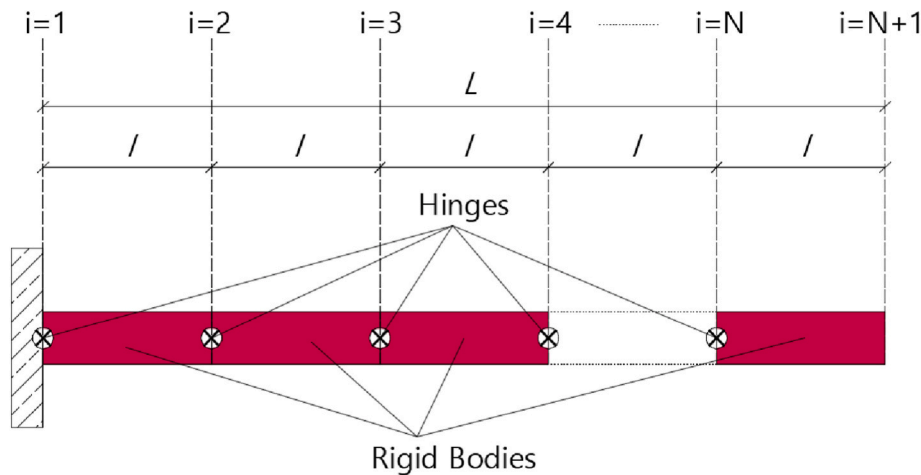

Fig. 2. Schematic view of cantilever beam used for torsional stiffness calculation.

The present torsional stiffness calculation process is limited with the Euler-Bernoulli beam theory assumptions (Donnell, 1976; Wang and Qin, 2019). Therefore, the value of uniformly distributed load to be used in the calculations should be determined considering the small slope angle assumption. In this regard, the authors determined the maximum load such that beam tip slope angle is equal to $\theta_0 = 0.20\,rad$, in which the Euler-Bernoulli beam theory provides relatively higher accuracy. Then, torque and relative rotation angles of hinges are calculated for various θ_0 values monotonically increasing inside the limits of $\theta_0 \in [0, 0.20$ rad$]$. It should be noted that calculations are carried out for 1 m width of the beam due to 2D simulation conditions in numerical analyses. A linear regression process is used to obtain approximated torsional stiffness values of each hinge. Obtained results are presented in Fig. 3 with the mean squared error (R^2) value for each regression. Case numbers represent the elastic plates used in Sections 4.1, 4.2, and 4.3, respectively. Hinges are numbered starting from the fixed point of the cantilever beam (Fig. 4d, Figs. 9c, and Fig. 14b). Results indicate that calculated K_Θ values are almost constant inside the predefined load

limits.

4. Validation results

In this section, the solution accuracy of the present numerical model is investigated firstly by an experimental setup based on dam-break wave impact on an elastic baffle in a wet bed. Then, two benchmark cases in the literature involving dam-break wave impact on an elastic sluice gate (Yilmaz et al., 2021) and dam-break flow with an elastic-gate (Antoci et al., 2007) are used for validation. Each validation case has different material properties and flow characteristics for solid and fluid sub-domains, respectively. Simulations are performed using NVIDIA GeForce GTX 1050 Ti GPU with Intel i7-8750H CPU and 16 GB RAM and, results are compared with experimental measurements and numerical computations obtained from various numerical models. Additionally, the effect of structural damping on numerical computations is investigated considering damping stiffness of hinges, calculated according to various predefined damping ratios (ζ) as follows;
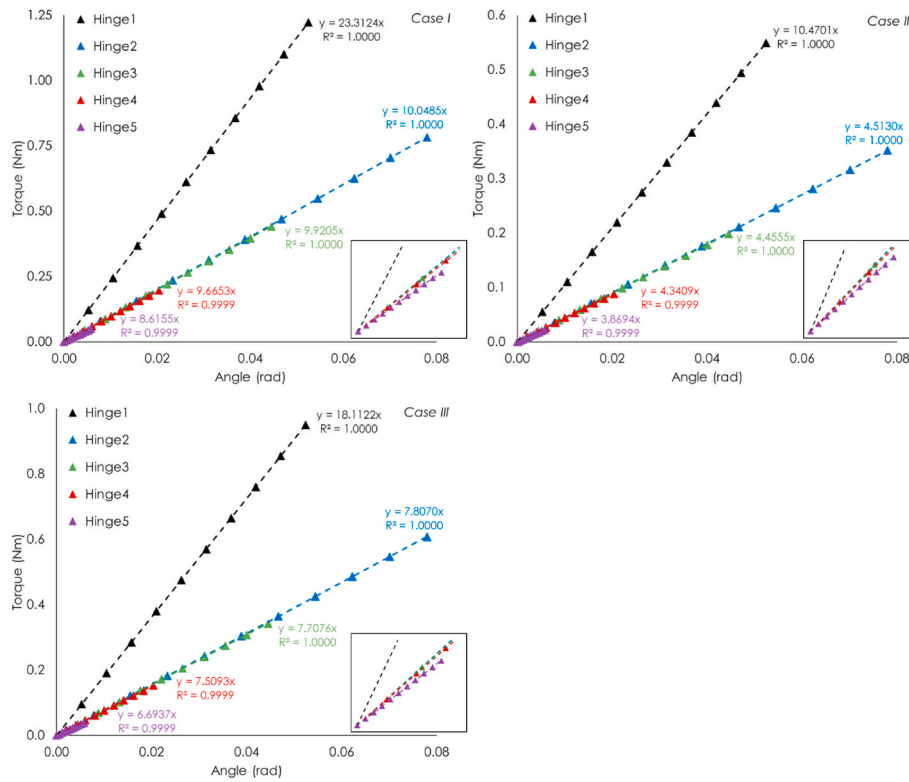
Fig. 3. Calculation of K_Θ of hinges using linear regression.
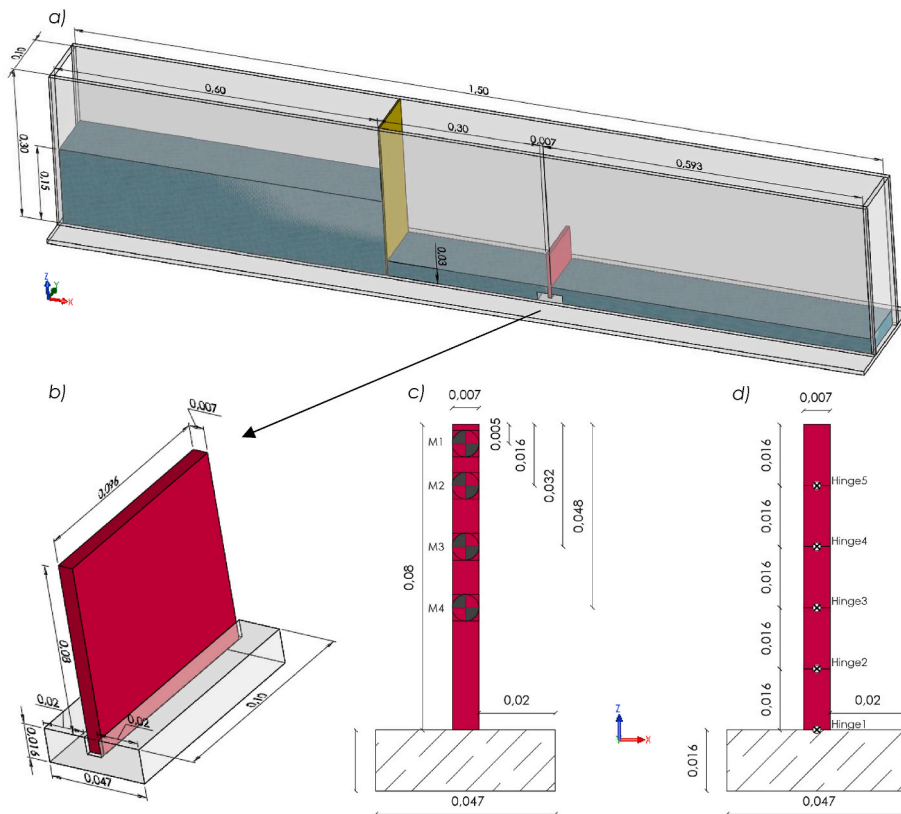

Fig. 4. Schematic view of *a)* experimental setup, *b)* baffle geometry, *c)* measurement points, and *d)* hinge locations (*units in m*).

$$K_\Omega = \zeta \, K_{\Omega C} \qquad (19)$$

where $K_{\Omega C}$ is the critical damping stiffness of hinges, which is $K_{\Omega C} = 2\sqrt{K_\Theta I}$.

4.1. Impact of a dam-break wave on elastic baffle in a wet bed

4.1.1. Experimental setup and measurement technique

A newly-designed experimental setup based on dam-break wave impact on an elastic baffle in a wet bed has been conducted to validate the present numerical model. Experiments have been carried out at Civil Engineering Hydraulics Laboratory of Iskenderun Technical University, Turkey, in a rectangular tank with 1.5 m in length, 0.3 m in height, and 0.1 m in width, made of 8 mm acrylic material. The rectangular tank is divided into two parts as upstream and downstream by a vertical rigid-gate with 3 mm thickness, located at a distance of 0.6 m from the tank entrance. The upstream and downstream initially are filled by water with $h_o = 0.15 \, m$ and $h_t = 0.03 \, m$ in height, respectively, to provide wet bed condition (Fig. 4a). A certain weight is attached to rigid-gate with a cable and is released from a certain height to generate an experimentally idealized dam-break flow. An elastic baffle made of rubber with 80 mm in height and 7 mm thickness is located at a distance of 0.9 m from tank entrance embedding into a rectangular foundation with 0.047 m in length and 0.016 m in height. The width of the baffle is chosen as 0.096 m to prevent possible friction between the baffle and tank walls (Fig. 4b).

In experiments, displacements of the baffle caused by water pressure are measured from digital video images using the image processing technique. With this technique, many researchers obtained sensitive experimental measurements in various dam-break flows (Kocaman and Ozmen-Cagatay, 2015; Ozmen-Cagatay et al., 2014) and hydroelasticity problems (Yilmaz et al., 2021). In this regard, experiments are recorded using a camera with 1920×1080 resolution in 240 frames per second. Four markers (M1-M4) are stuck along the front face of the elastic baffle to measure nodal displacements caused by water pressure (Fig. 4c). Both upstream and downstream are colored using a dye to better identify the air-water-solid interfaces in the video images. The details of the measurement technique used in this paper can be found in the work of Yilmaz et al. (2021).

Young's modulus of baffle used in the experiment is determined using an analytical solution of Euler-Bernoulli beam theory (*Eq. (15)*). At first, the displacements of three specified points on the baffle section under self-weight are measured from digital video images. A marker with 0.02 m in diameter is used as a predetermined reference length to convert the pixels into metric units. Measurement results are shown in Fig. 5. However, it should be noted that displacements, presented in Fig. 5, are measured from the predefined reference axis, corresponding

to the upper surface of the baffle in the initial position. These values are converted into nodal deflections, used in Young's modulus calculations, by subtracting half of the baffle thickness from itself. Calculation results are presented in Table 1. Obtained results demonstrate that using Young's Modulus of the plate as 5.7 MPa will be a reasonable approximation.

4.1.2. Comparisons of experimental measurements and numerical computations

In the present numerical model, the solid sub-domain of the phenomenon is modeled using five rigid bodies attached by hinges with torsional stiffness (Fig. 4d). These hinges are allowed to rotate only about the y-axis in 2D analysis. Each rigid body has the value of $l = 0.016 \, m$ length, $m = 0.14 \, kg$ mass, and $I_{yy} = 1.25183E\text{-}05 \, kg \, m^2$ moment of inertia, where the subscript y represents the axis in the baffle width direction (Fig. 4). The torsional stiffness values of related hinges are calculated using the regression process described in Section 3 (*Case I in Fig. 3*). Obtained results are presented in Table 2 with other simulation parameters. However, it should be noted that related torsional stiffness, mass, and moment of inertia values are calculated for 1 m width of baffle due to 2D simulation conditions.

The numerical simulation is performed for 1.5 s using the parameters presented in Table 2 and, obtained results are illustrated in Fig. 6 comparing with the experimental sequences. Shortly after the sudden removal of the rigid-gate, it is observed that initial upstream water starts to drag still tail-water, resulting in a jet formation moving downstream direction. Kocaman and Ozmen-Cagatay (2015) and Ozmen-Cagatay and Kocaman (2010) reported similar behavior of the dam break flow in wet bed at initial stages. The flood wave breaks nearly about the baffle location and, a sudden displacement on the solid body is observed, resulting from highly dynamic first contact. Then, a relaxation occurs on the baffle and, a part of the wave starts to overtop the elastic baffle, while another part reflects towards upstream. After that point, the static impacts become more dominant on the baffle. By the decreasing upstream water level due to finite reservoir length, the displacements on the baffle start to decrease simultaneously. The authors consider that the present experimental phenomenon is a suitable benchmark case for numerical models used in hydroelasticity analysis by dynamics it contains.

Due to the highly dynamic characteristics of the phenomenon, experiments were repeated two times. Obtained displacement measurements are presented in Fig. 7 comparing with numerical computations. Results show that the present model computations are in well-agreement with the main displacement characteristics of the baffle. However, it is observed that the peak displacement caused by the first impact is higher in numerical computations. Authors consider that this situation may be caused by differences in wave-front evolution between experimental and
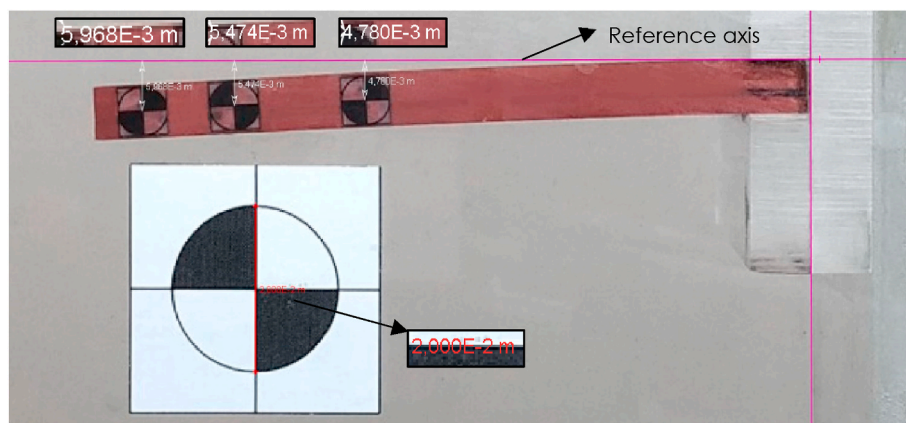

Fig. 5. Measured baffle displacements (*units in m*).

Table 1

Calculated Young's modulus values.

Measurement point	Location from the free end (m)	Displacement from reference axis (m)	Deflection on measurement points (m)	ρ (kg/m³)	Calculated E (MPa)
1	0.005	0.005968	0.002468	1250	5.71
2	0.016	0.005474	0.001974		5.72
3	0.032	0.004780	0.001280		5.71

Table 2

Simulation parameters and torsional stiffness values of hinges.

WCSPH Simulation parameters	
Initial particle distance (d_p)	1 mm
Particle resolution (h_0/d_p)	150
Smoothing length (h)	1.2dp
Artificial viscosity constant (α)	0.04
δ-SPH constant ($δ_φ$)	0.1
Torsional stiffness values for hinges (Nm/rad)	
Hinge1	23.3124
Hinge2	10.0485
Hinge3	9.9205
Hinge4	9.6653
Hinge5	8.6155

numerical results. Also, it should be noted that there are gaps between

the baffle and tank walls in the experimental setup to prevent possible frictions and, liquid leakage through those gaps has been observed during experiments, which can cause pressure reductions on the baffle surface.

Fig. 8 shows the displacement comparisons between the experimental measurements and present model results computed according to various damping ratios in the range of 0% and 30%. Results indicate that damping ratios in considering range have no notable effect on the numerical computations except minor oscillation differences.

4.2. Dam-break wave impact on elastic sluice gate

Phenomenon based on dam-break wave impact on an elastic sluice gate is firstly studied experimentally and numerically by Yilmaz et al. (2021). A schematic view of the experimental setup is shown in Fig. 9a. An initial water column with 0.5 m in length and 0.2 m (h_0) in height is
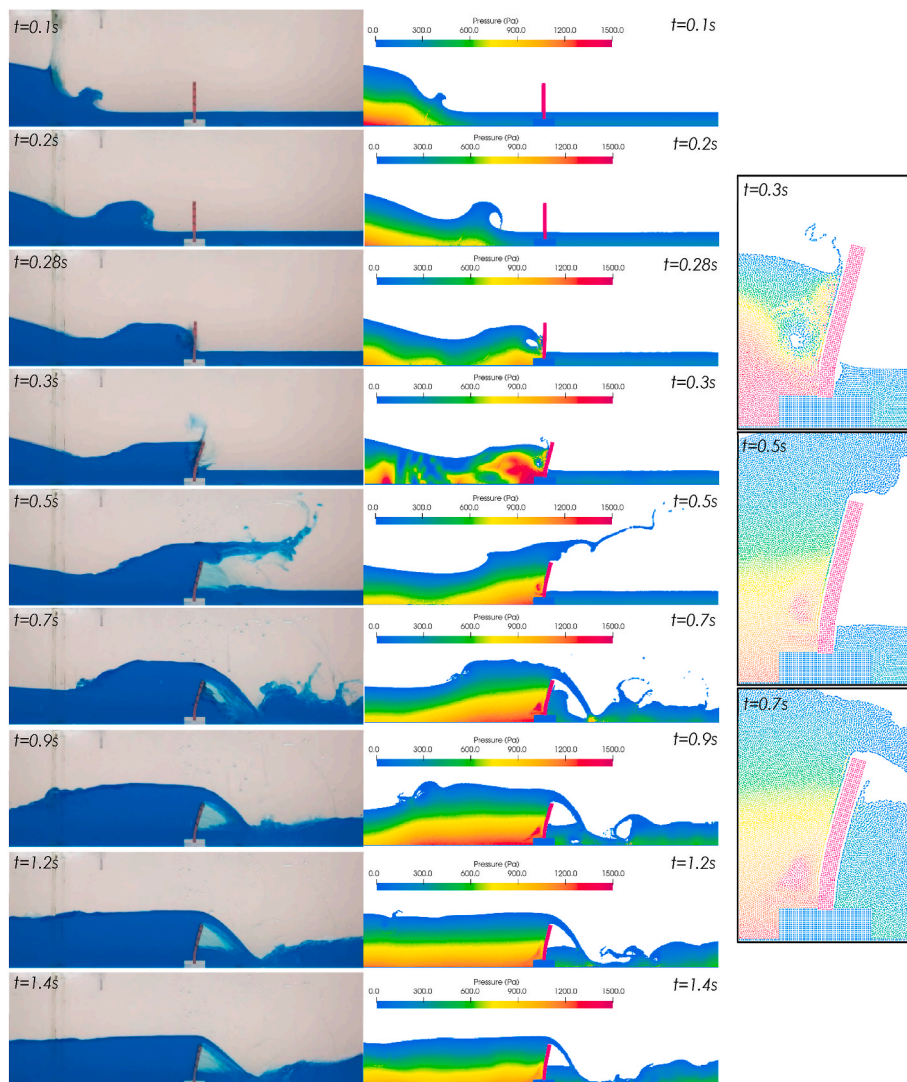

Fig. 6. Comparison of experimental and numerical sequences (without damping) at various times.
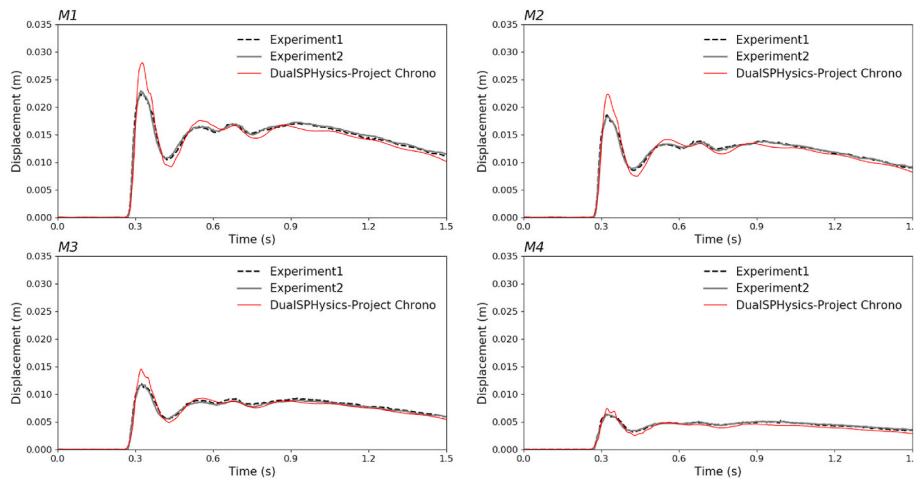
Fig. 7. Displacement comparisons of the present model computations without damping at measurement points *(M1-M4)*.
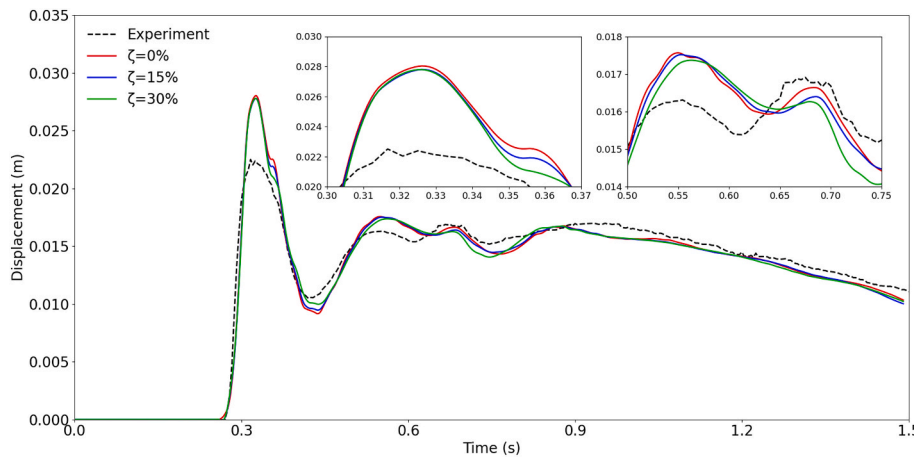

Fig. 8. Comparisons of experimental measurements with present model results computed according to various damping ratios *at M1*.

located at the entrance of a rectangular channel with 1.508 m in length, 0.3 m in height, and 0.1 m in width. The rectangular channel is divided into two parts using a vertical rigid gate located at the end of the initial water column. An elastic sluice gate, made of a rubber-like material with density $\rho = 1250\ kg/m^3$, Young's modulus $E = 4\ MPa$, 0.125 m in height, 0.007 m in thickness, and 0.097 m in width are located at 0.8 m from the channel entrance.

In the computational setup, elastic sluice gate is modeled using five rigid bodies attached by hinges with torsional stiffness (Fig. 9c). Each body has $l = 0.025\ m$ length and $m = 0.\ 21875\ kg$ mass, and $I_{yy} = 4.64661E\text{-}05\ kg\ m^2$ moment of inertia values. Hinges are allowed to

rotate only about the y-axis by torsional stiffness values calculated using the regression process described in Section 3 *(Case II in Fig. 3)*. These values are presented in Table 3 with other simulation parameters. All those values are calculated for 1 m plate width considering 2D simulation conditions.

Fig. 10 shows experimental and numerical sequences at various time steps. By sudden removal of rigid-gate, dam-break wave-front starts to propagate towards downstream. The first contact between the wave-front and elastic sluice gate occurs at about t = 0.23 s. This impact causes a sudden displacement and a relaxation subsequently on the gate. By the second impact, the generation of highly rotational flow with a hydraulic jump and negative bore is observed, causing oscillations on the plate. Then, static impacts become dominant on plate displacements decreasing simultaneously with water level behind the gate.

Fig. 11 shows comparisons of plate displacements at four measurement points given in Fig. 9b. Present model computations are compared with experimental measurements and SPH-FEM results of Yilmaz et al. (2021). Both works use WCSPH for modeling fluid motion, but there are some differences between these two models theoretically (e.g. kernel function and treatment of density fluctuations) and parametrically (e.g. particle resolution and smoothing length). Moreover, Yilmaz et al. (2021) used a FEM formulation for modeling structural dynamics of the phenomenon and coupled it numerically with the fluid model using a penalty-based formulation. It is observed that there is a well-agreement between the present model computations and the experimental and numerical results of Yilmaz et al. (2021). However, after $t = 0.8\ s$ time,
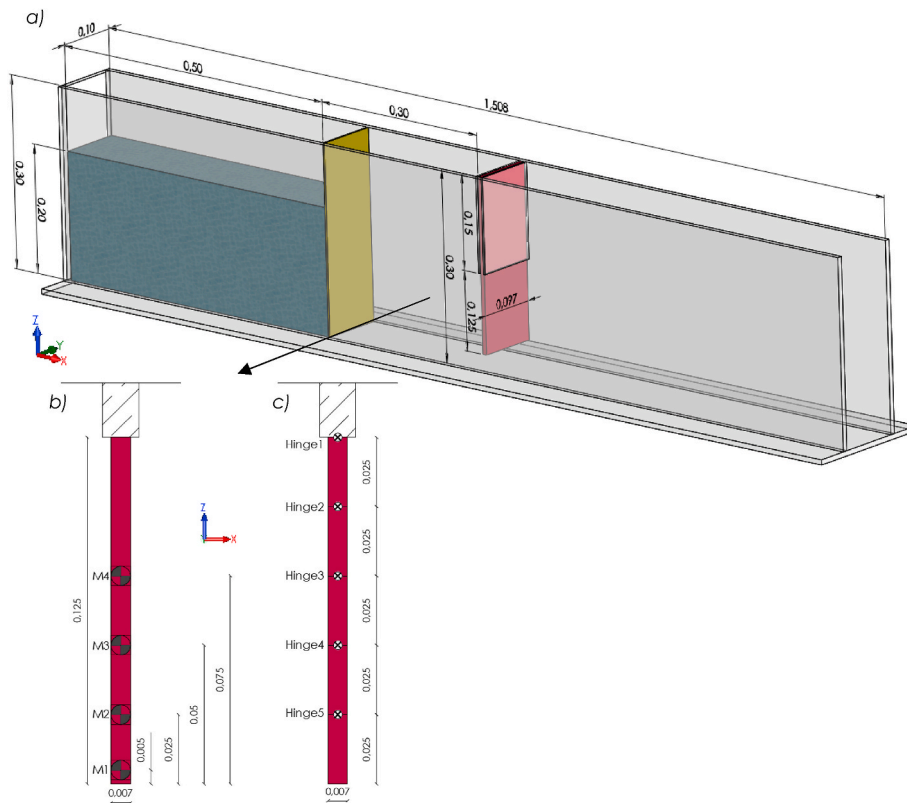
Table 3
Simulation parameters and torsional stiffness values of hinges.

WCSPH Simulation parameters	
Initial particle distance (d_p)	1 mm
Particle resolution (h_0/d_p)	200
Smoothing length (h)	$1.35 dp$
Artificial viscosity constant (α)	0.03
δ-SPH constant (δ_φ)	0.1
Torsional stiffness values for hinges (Nm/rad)	
Hinge1	10.4701
Hinge2	4.5130
Hinge3	4.4555
Hinge4	4.3409
Hinge5	3.8694

Fig. 9. Schematic view of *a)* experimental setup, *b)* measurement points, and *c)* hinge locations (*units in m*).
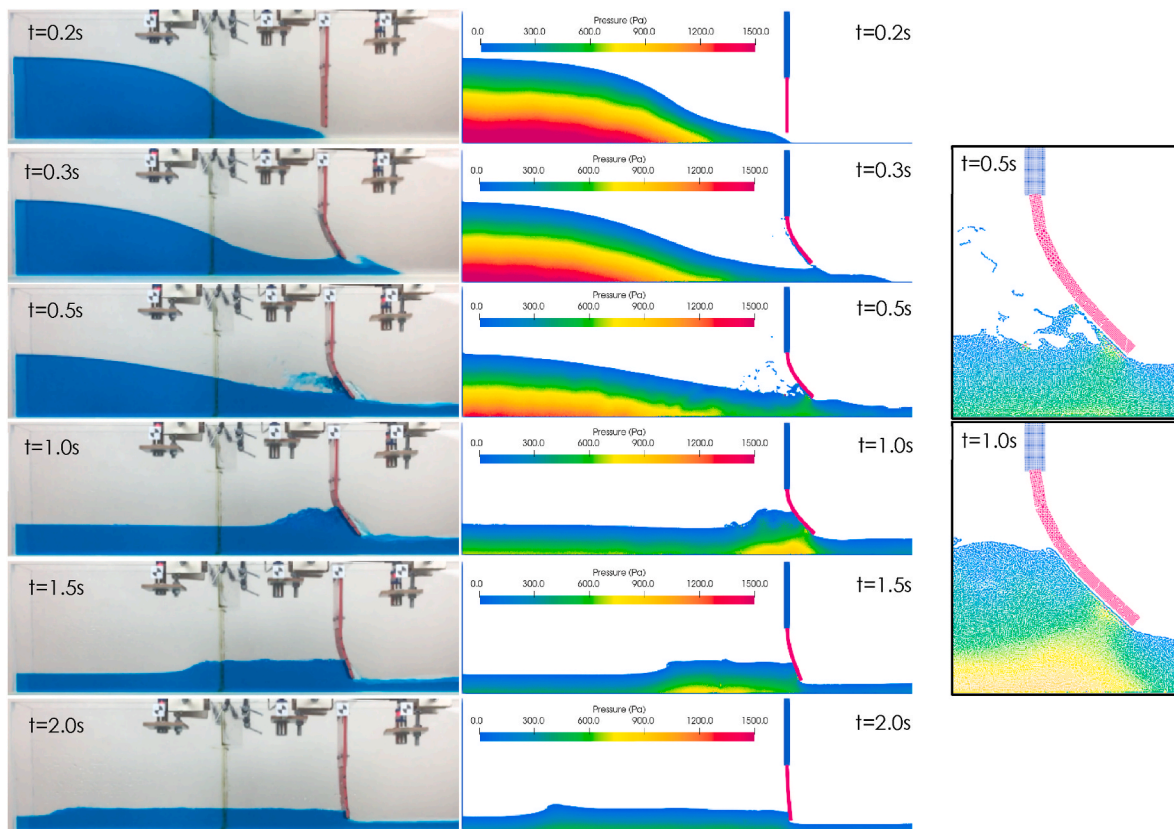

Fig. 10. Comparison of experimental and numerical sequences (without damping) at various times.
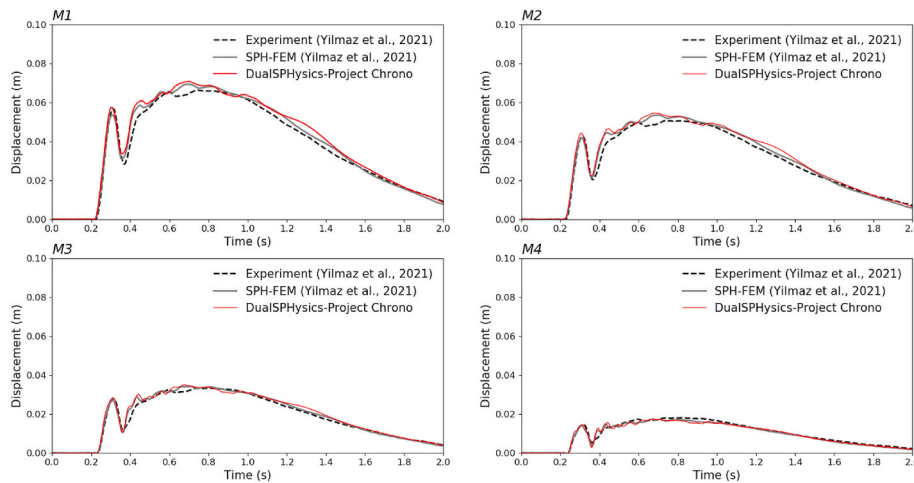
Fig. 11. Displacement comparisons of the present model computations without damping at measurement points (M1-M4).

minor deviations in displacement computation of the present model drawn attention. In mentioned time interval, the evolution of a chaotic fluid motion with hydraulic jump is observed near the fluid-solid interface, which may be a possible reason for deviations on the solid plate.
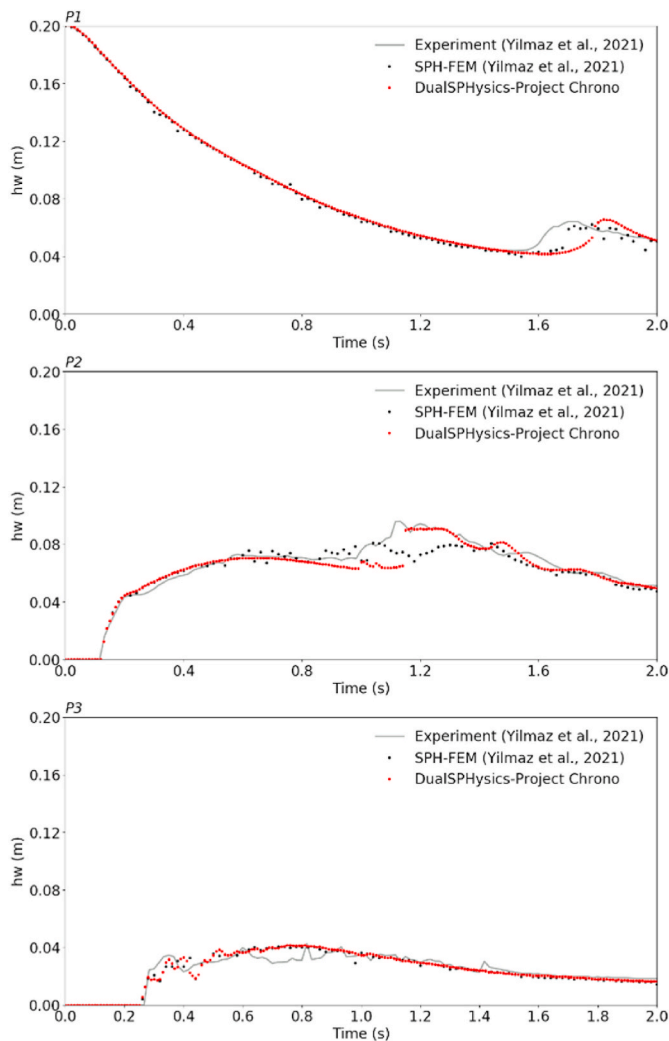

Fig. 12. Water level comparisons of the present model computations (without damping) at measurement points *(P1–P3)*.

Fig. 12 illustrates water level comparisons at three measurement points *(P1–P3)* located at 0.35 m, 0.65 m, and 0.95 m from the channel entrance, respectively. At P1, the present model provides quite close results compared with experimental measurements and SPH-FEM model results of Yilmaz et al. (2021) till the reflection wave arrives. After that point, there is a phase difference in wave-front evolution between the experimental measurements and both numerical model computations. At the P2 and P3, there is a well-agreement between both two numerical model results. Compared to experimental measurements, wave-crest in numerical computations is not as apparent as an experimental one at P2. Also, fluctuations in water levels occurring at P3 are not captured strictly by both two numerical models. However, it is considered that the present numerical model provides reasonable accuracy in water level computations when compared to experimental measurements.

Fig. 13 shows the comparison of the present model results computed according to predefined damping ratios with experimental measurements. Results indicate that related damping ratios have no significant effect on numerical displacements until t = 0.4 s. After that point, the chaotic fluid motion mentioned above becomes dominant and, deviations and oscillations are observed in gate displacement computations depending on the damping ratio used. Authors have also encountered a parametric sensitivity (e.g. smoothing length, artificial viscosity constant, and initial particle resolution) during numerical analyses with constant damping ratios, resulting in similar deviations and oscillations in the related time interval. Therefore, the authors consider that differences in the gate displacement computations after t = 0.4 s are caused by related sensitivity in the fluid motion rather than structural damping effect and the dynamics of the problem can be investigated by a detailed parametric study or by testing different coupling schemes.

4.3. Dam-break flow with an elastic gate

Phenomenon based on the deformation of the elastic gate under the water pressure is firstly studied experimentally and numerically by Antoci et al. (2007) and later modeled numerically by many researchers (Yang et al., 2012; Zhan et al., 2019). The initial water body, with 0.14 m in height *(h₀)*, 0.1 m in length, and 0.1 m in width, is confined by an elastic plate with 0.079 m in length, 0.098 m in width, and 0.005 m in thickness. While the upper part of the gate is attached to a rigid wall, the lower one can deform freely by water pressure. Initially, the free end of the plate is confined by rigid support and, the water body is in hydrostatic condition. The schematic view of the experimental setup is shown in Fig. 14a.

In the present numerical model, elastic plate, with density $\rho = 1100$ kg/m^3 and Young's modulus $E = 12$ MPa, is divided into five rigid bodies with $l = 0.0158$ m in length and $m = 0.0869$ kg in mass (Fig. 14b). Each
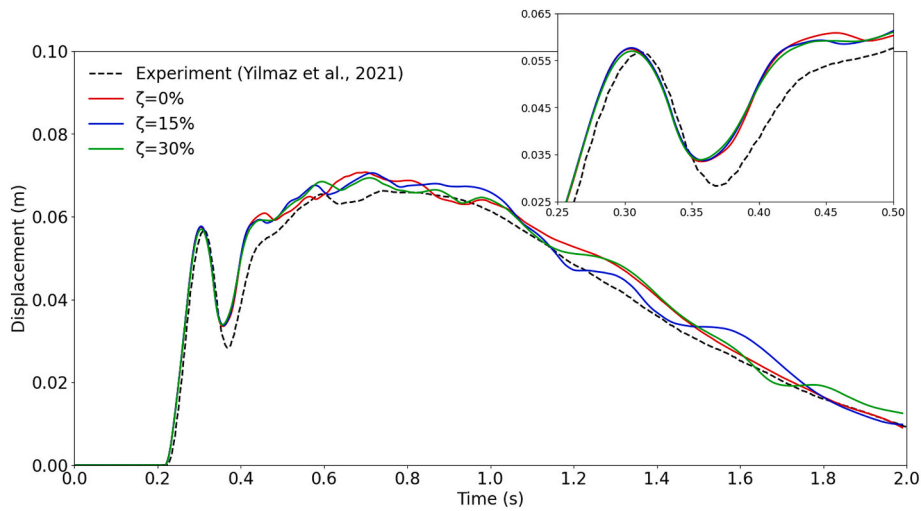
Fig. 13. Comparisons of experimental measurements with present model results computed according to various damping ratios at M1.
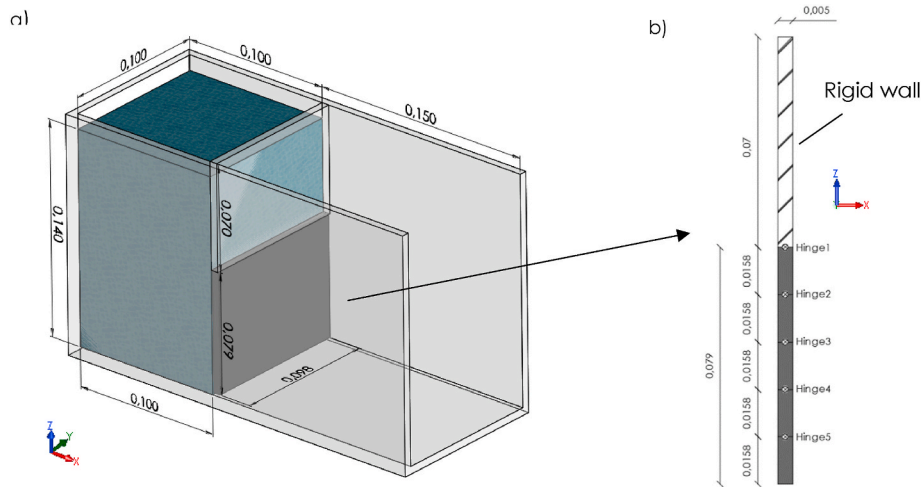

Fig. 14. Schematic view of *a)* the experimental setup and *b)* hinge locations *(units in m)*.

body is attached by hinges allowed to rotate only about the y-axis. The moment of inertia of each body is set to $I_{yy} = 7.41228E\text{-}06 \ kg \ m^2$ concerning rotation point. Torsional stiffness values of hinges are calculated using the regression process described in Section 3 for 1 m gate width in 2D simulation condition *(Case III in Fig. 3)*. Obtained results are presented in Table 4.

Numerical simulation is performed for 0.4 s and, results at various times are illustrated in Fig. 15 with pressure contour. With the sudden release of the initial water body, the elastic gate starts to deform by

Table 4
Simulation parameters and torsional stiffness values of hinges.

WCSPH Simulation parameters	
Initial particle distance (d_p)	0.5 mm
Particle resolution (h_0/d_p)	280
Smoothing length (h)	1.2dp
Artificial viscosity constant (α)	0.02
δ-SPH constant (δ_φ)	0.1
Torsional stiffness values for hinges (Nm/rad)	
Hinge1	18.1122
Hinge2	7.8070
Hinge3	7.7076
Hinge4	7.5093
Hinge5	6.6937

water pressure and reaches peak displacement in a short time. After that peak point, a relaxation on the gate is observed and, displacement values start to decrease. As water pressure becomes dominant once again, relaxation gradient decreases over time and, a slight displacement increase on the gate is observed.

Fig. 16a shows the comparisons of the time history of displacements at the gate tip point. The present model computations without damping are compared with the experimental and numerical results of Antoci et al. (2007), SPH-FEM model results of Yang et al. (2012), and TL-WCSPH model results of Zhan et al. (2019). Antoci et al. (2007) and Zhan et al. (2019) use hypoelastic and hyperelastic material models for the solid phase of the problem, respectively. Yang et al. (2012) use both linear and hyperelastic material models. In this work, the analytical solution used to calculate torsional stiffness values of hinges is based on linear elastic theory. It can be seen that numerical models using hyperelastic and hypoelastic material models reproduce experimental measurements more accurately. But, the results of the SPH-FEM model of Yang et al. (2012) based on linear elastic theory and the present numerical model are far from the agreement compared to experimental measurements and other numerical model results. Yang et al. (2012) compared numerical results obtained linear elastic and hyperelastic material models in their work and explained the difference between computations by less stiff behavior of hyperelastic models under large
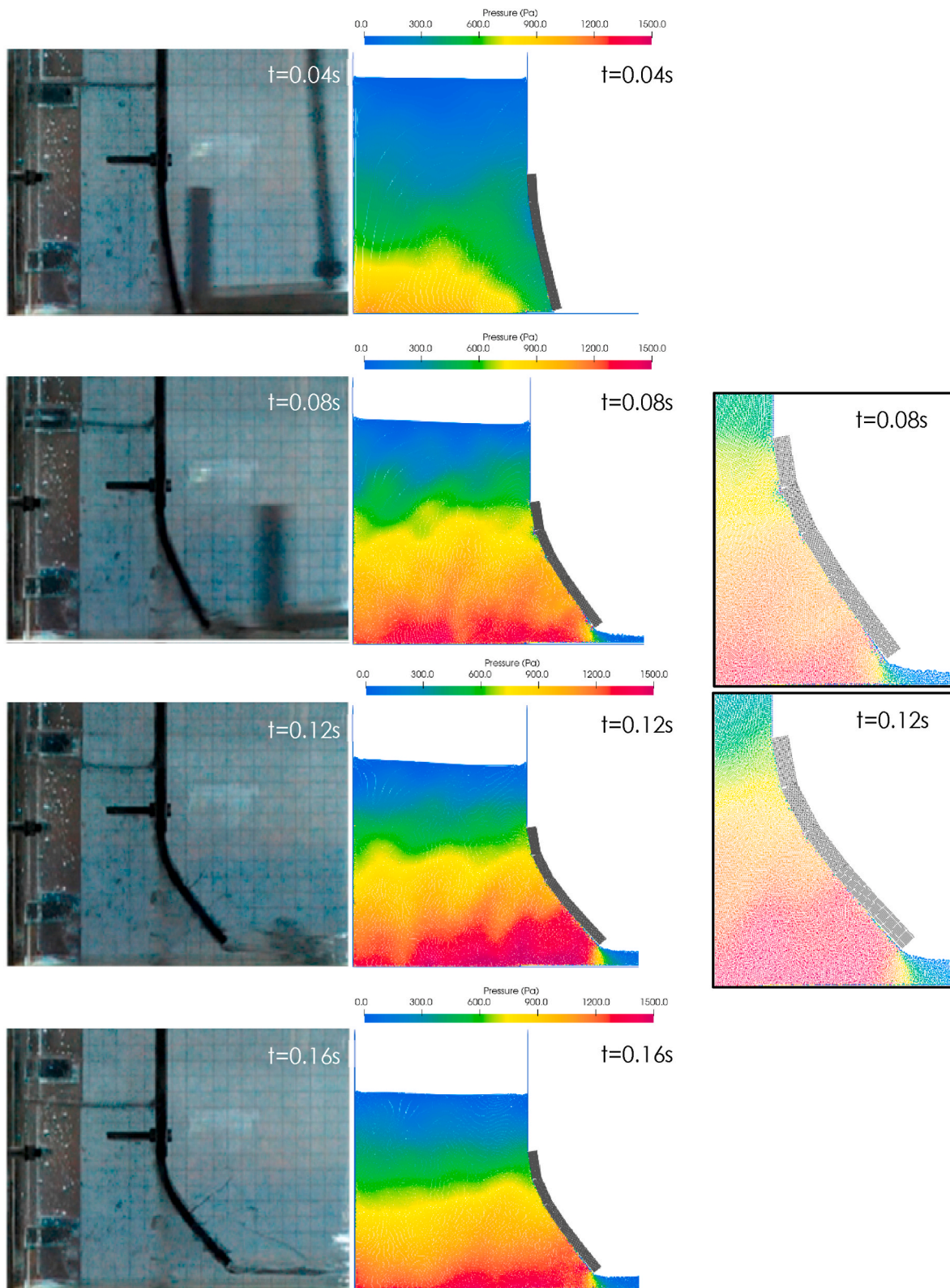
Fig. 15. Comparison of experimental and numerical sequences (without damping) at various times.

deformations. However, results also demonstrate that there is a well-agreement between present model computations and the SPH-FEM model results of Yang et al. (2012) obtained from the linear elastic material model.

Fig. 16b shows the comparison of the present model results computed according to predefined damping ratios with the computation of Yang et al. (2012). Results indicate that predefined damping ratios have no notable effect on the gate displacements. Furthermore, it is observed that the damping effect is more limited in this case compared to the previous two benchmark cases. This can be found reasonable considering the domination of static impacts in the present case.
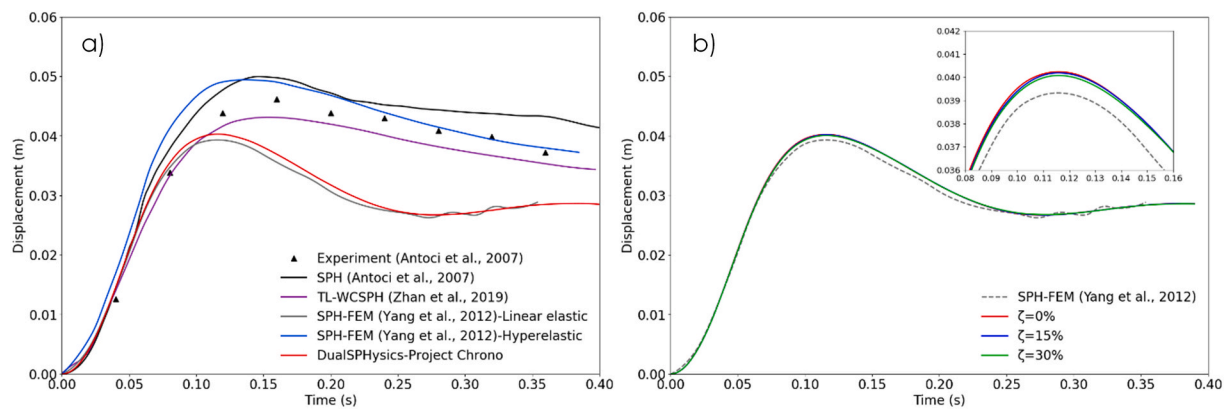
Fig. 16. Comparisons of gate tip point displacements.

5. Conclusions

This paper presents an implementation of DualSPHysics-Project Chrono coupling to hydroelasticity problems involving free-surface flows and deformable elastic boundaries. In the present coupling scheme, the fluid sub-domain is modeled by the WCSPH formulation of DualSPHysics, while the solid sub-domain, consisting of rigid bodies attached by hinges with torsional and damping stiffness, is simulated by Project Chrono. Torsional stiffness values of hinges, calculated by an analytical solution of Euler-Bernoulli beam theory, are used to approximate the rigid multibody system to mechanical characteristics of solid sub-domain.

The accuracy and stability of the present model are investigated using a newly-designed experimental setup and two benchmark cases in the literature. In all that cases, it is observed that the present numerical model computations showed a well-agreement with the results obtained from experimental measurements and other numerical model computations. Furthermore, the effect of structural damping is investigated considering damping stiffness values of hinges calculated according to predefined damping ratios. Obtained results indicate that structural damping has no notable effect on numerical computations of present benchmark cases.

In the present numerical model, an application of DBC is used for fluid-rigid body coupling. This scheme provides computational simplicity since solid particles are calculated inside the same loops as fluid particles (Crespo et al., 2007). However, DBC presents some drawbacks, such as the unphysical gap formation between the fluid and solid particles and pressure fluctuations near the fluid-solid interface. The authors consider that implementing an enhanced formulation for coupling (e.g. Modified Dynamic Boundary Condition (English et al., 2021)) in the present model can increase the solution accuracy and provide a more smooth pressure field around the coupling.

In all validation cases, the solid sub-domain has been modeled using five rigid bodies in equal length. Even the reasonable accuracy is captured with a limited number of rigid bodies, geometric discontinuities (gaps at attachment points) caused by high relative rotation rates of rigid bodies can appear depending on the increase in displacements. Theoretically, it is expected that an increase in the number of the rigid body will improve model accuracy and mentioned discontinuities. In this regard, the authors consider that a detailed parametric study can be carried out to investigate the effects of different rigid body configurations on solution accuracy and find optimal design parameters (e.g. rigid body number and length).

In this work, the torsional stiffness of hinges is calculated by a regression process based on the Euler-Bernoulli beam theory of a cantilever beam under a uniformly distributed load in the limited deflection range. Although this approximation provides reasonable accuracy for hydroelasticity cases used in this work, the calculation

process of the torsional stiffness values of hinges can be optimized using different theories for the solid sub-domains of the phenomenon that undergo large and nonlinear deflections. Also, all validation cases used in the present paper have the same boundary conditions. The solution accuracy of the present model can also be investigated for solid sub-domains with different boundary conditions by modifying static and kinematic equations.

The present numerical model offers computational simplicity and high efficiency with GPU-accelerated analysis capability (Canelas et al., 2018; Domínguez et al., 2021). With these capabilities allowing numerical modeling of large and complex systems, authors consider that the present model can be employed easily in 3D analyses of hydroelasticity problems with high particle numbers by increasing hinges' degree of freedom.

CRediT authorship contribution statement

Ada Yilmaz: Conceptualization, Investigation, Software, Writing – original draft, Writing – review & editing. **Selahattin Kocaman:** Conceptualization, Supervision, Writing – original draft, Writing – review & editing. **Mustafa Demirci:** Conceptualization, Supervision, Writing – original draft.

Declaration of competing interest

The authors declare that they have no known competing financial interests or personal relationships that could have appeared to influence the work reported in this paper.

References

Altomare, C., Domínguez, J.M., Crespo, A.J.C., González-Cao, J., Suzuki, T., Gómez-Gesteira, M., Troch, P., 2017. Long-crested wave generation and absorption for SPH-based DualSPHysics model. Coast. Eng. 127, 37–54. https://doi.org/10.1016/j.coastaleng.2017.06.004.

Antoci, C., Gallati, M., Sibilla, S., 2007. Numerical simulation of fluid-structure interaction by SPH. Comput. Struct. 85, 879–890. https://doi.org/10.1016/j.compstruc.2007.01.002.

Areu-Rangel, O.S., Hernández-Fontes, J.V., Silva, R., Esperança, P.T.T., Klapp, J., 2021. Green water loads using the wet dam-break method and SPH. Ocean Eng. 219 https://doi.org/10.1016/j.oceaneng.2020.108392.

Bašić, J., Degiuli, N., Malenica, Š., Ban, D., 2020. Lagrangian finite-difference method for predicting green water loadings. Ocean Eng. 209, 107533 https://doi.org/10.1016/j.oceaneng.2020.107533.

Batchelor, G.K., 1974. An Introduction to Fluid Mechanics. Cambridge University Press, UK.

Brito, M., Canelas, R.B., Ferreira, R.M.L., 2016. Coupling between DualSPHysics and Chrono- Engine : towards large scale HPC multiphysics simulations. 11th Int. SPHERIC Work. 6–7.

Brito, M., Canelas, R.B., García-Feal, O., Domínguez, J.M., Crespo, A.J.C., Ferreira, R.M.L., Neves, M.G., Teixeira, L., 2020. A numerical tool for modelling oscillating wave surge converter with nonlinear mechanical constraints. Renew. Energy 146, 2024–2043. https://doi.org/10.1016/j.renene.2019.08.034.

Canelas, R.B., Brito, M., Feal, O.G., Domínguez, J.M., Crespo, A.J.C., 2018. Extending DualSPHysics with a differential variational inequality: modeling fluid-mechanism interaction. Appl. Ocean Res. 76, 88–97. https://doi.org/10.1016/j. apor.2018.04.015.

Canelas, R.B., Dominguez, J.M., Crespo, A.J.C., Gomez-Gesteira, M., Ferreira, R.M.L., 2015. A Smooth Particle Hydrodynamics discretization for the modelling of free surface flows and rigid body dynamics. Int. J. Numer. Methods Fluid. 78, 581–593. https://doi.org/10.1002/fld.4031.

Colicchio, G., Colagrossi, A., Greco, M., Landrini, M., 2002. Free-surface flow after a dam break: a comparative study. Ship Technol. Res. 49, 95–104.

Crespo, A.J.C., Domínguez, J.M., Rogers, B.D., Gómez-Gesteira, M., Longshaw, S., Canelas, R., Vacondio, R., Barreiro, A., García-Feal, O., 2015. DualSPHysics: open-source parallel CFD solver based on smoothed particle hydrodynamics (SPH). Comput. Phys. Commun. 187, 204–216. https://doi.org/10.1016/j. cpc.2014.10.004.

Crespo, A.J.C., Gomez-Gesteira, M., Dalrymple, R.A., 2007. Boundary conditions generated by dynamic particles in SPH methods. Comput. Mater. Continua (CMC) 5, 173–184.

Crespo, A.J.C., Gómez-Gesteira, M., Dalrymple, R.A., 2008. Modeling dam break behavior over a wet bed by a SPH technique. J. Waterw. Port, Coast. Ocean Eng. 134, 313–320. https://doi.org/10.1061/(ASCE)0733-950X, 2008)134:6(313.

Domínguez, J.M., Crespo, A.J.C., Gómez-Gesteira, M., 2013. Optimization strategies for CPU and GPU implementations of a smoothed particle hydrodynamics method. Comput. Phys. Commun. 184, 617–627. https://doi.org/10.1016/j. cpc.2012.10.015.

Domínguez, J.M., Fourtakas, G., Altomare, C., Canelas, R.B., Tafuni, A., García-Feal, O., Martínez-Estévez, I., Mokos, A., Vacondio, R., Crespo, A.J.C., Rogers, B.D., Stansby, P.K., Gomez-Gesteira, M., 2021. DualSPHysics : from fluid dynamics to multiphysics problems. Comput. Part. Mechan. https://doi.org/10.1007/s40571-021-00404-2.

Donnell, L.H., 1976. Beams, Plates, and Shells. McGraw-Hill, New York.

English, A., Domínguez, J.M., Vacondio, R., Crespo, A.J.C., Stansby, P.K., Lind, S.J., Chiapponi, L., Gómez-Gesteira, M., 2021. Modified dynamic boundary conditions (mDBC) for general-purpose smoothed particle hydrodynamics (SPH): application to tank sloshing, dam break and fish pass problems. Comput. Part. Mechan. https://doi. org/10.1007/s40571-021-00403-3.

Fourtakas, G., Dominguez, J.M., Vacondio, R., Rogers, B.D., 2019. Local uniform stencil (LUST) boundary condition for arbitrary 3-D boundaries in parallel smoothed particle hydrodynamics (SPH) models. Comput. Fluids 190, 346–361. https://doi. org/10.1016/j.compfluid.2019.06.009.

Gingold, R., Monaghan, J.J., 1977. Smoothed particle hydrodynamics: theory and application to non-spherical stars. Mon. Not. Roy. Astron. Soc. 181, 375–189.

Gomez-Gesteira, M., Rogers, B.D., Dalrymple, R.A., Crespo, A.J.C., 2010. State-of-the-art of classical SPH for free-surface flows. J. Hydraul. Res. 48, 6–27. https://doi.org/10.1080/00221686.2010.9641242.

Groeneboom, P.H.L., Cartwright, B.K., 2010. Hydrodynamics and fluid-structure interaction by coupled SPH-FE method. J. Hydraul. Res. 48, 61–73. https://doi.org/10.3826/jhr.2010.0004.

Han, L., Hu, X., 2018. SPH modeling of fluid-structure interaction. J. Hydrodyn. 30, 62–69. https://doi.org/10.1007/s42241-018-0006-9.

Han, X., Dong, S., 2020. Interaction of solitary wave with submerged breakwater by smoothed particle hydrodynamics. Ocean Eng. 216, 108108 https://doi.org/10.1016/j.oceaneng.2020.108108.

He, J., Tofighi, N., Yildiz, M., Lei, J., Suleman, A., 2017. A coupled WC-TL SPH method for simulation of hydroelastic problems. Int. J. Comput. Fluid Dynam. 31, 174–187. https://doi.org/10.1080/10618562.2017.1324149.

Howell, L.L., 2001. Compliant Mechanisms. John Wiley & Sons, New York.

Howell, L.L., Midha, A., 1994. A method for the design of compliant mechanisms with small-length flexural pivots. J. Mech. Des. Trans. ASME 116, 280–290. https://doi. org/10.1115/1.2919359.

Iglesias, A.S., Rojas, L.P., Rodríguez, R.Z., 2004. Simulation of anti-roll tanks and sloshing type problems with smoothed particle hydrodynamics. Ocean Eng. 31, 1169–1192. https://doi.org/10.1016/j.oceaneng.2003.09.002.

Khayyer, A., Gotoh, H., Falahaty, H., Shimizu, Y., 2018. An enhanced ISPH–SPH coupled method for simulation of incompressible fluid–elastic structure interactions. Comput. Phys. Commun. 232, 139–164. https://doi.org/10.1016/j. cpc.2018.05.012.

Khayyer, A., Shimizu, Y., Gotoh, H., Hattori, S., 2021. Multi-resolution ISPH-SPH for accurate and efficient simulation of hydroelastic fluid-structure interactions in ocean engineering. Ocean Eng. https://doi.org/10.1016/j.oceaneng.2021.108652, 108652.

Khayyer, A., Tsuruta, N., Shimizu, Y., Gotoh, H., 2019. Multi-resolution MPS for incompressible fluid-elastic structure interactions in ocean engineering. Appl. Ocean Res. 82, 397–414. https://doi.org/10.1016/j.apor.2018.10.020.

Kocaman, S., Ozmen-Cagatay, H., 2015. Investigation of dam-break induced shock waves impact on a vertical wall. J. Hydrol. 525, 1–12. https://doi.org/10.1016/j. jhydrol.2015.03.040.

Li, Z., Leduc, J., Nunez-Ramirez, J., Combescure, A., Marongiu, J.C., 2015. A non-intrusive partitioned approach to couple smoothed particle hydrodynamics and finite element methods for transient fluid-structure interaction problems with large interface motion. Comput. Mech. 55, 697–718. https://doi.org/10.1007/s00466-015-1131-8.

Liu, M. Bin, Shao, J.R., Li, H.Q., 2013. Numerical simulation of hydro-elastic problems with smoothed particle hydrodynamics method. J. Hydrodyn. 25, 673–682. https://doi.org/10.1016/S1001-6058(13)60412-6.

Liu, Z., Wang, Y., Hua, X., 2020. Numerical studies and proposal of design equations on cylindrical oscillating wave surge converters under regular waves using SPH. Energy Convers. Manag. 203, 112242 https://doi.org/10.1016/j.enconman.2019.112242.

Lucy, L.B., 1977. A numerical approach to the testing of the fission hypothesis. Astron. J. 82, 1013–1024.

Macia, F., Antuono, M., Colagrossi, A., 2011. Benefits of using a Wendland kernel for free-surface flows. In: 6th International SPHERIC Workshop. Hamburg, Germany, pp. 30–37.

Mazhar, H., Heyn, T., Negrut, D., Tasora, A., 2015. Using Nesterov's method to accelerate multibody dynamics with friction and contact. ACM Trans. Graph. 34 https://doi.org/10.1145/2735627.

Molteni, D., Colagrossi, A., 2009. A simple procedure to improve the pressure evaluation in hydrodynamic context using the SPH. Comput. Phys. Commun. 180, 861–872. https://doi.org/10.1016/j.cpc.2008.12.004.

Monaghan, J.J., 2005. Smoothed particle hydrodynamics. Rep. Prog. Phys. 68, 1703–1759. https://doi.org/10.1088/0034-4885/68/8/R01.

Monaghan, J.J., 1994. Simulating free surface flows with SPH. J. Comput. Phys. 110, 399–406.

Monaghan, J.J., 1992. Smoothed particle hydrodynamics. Annu. Rev. Astron. Astrophys. 30, 543–574.

Monaghan, J.J., Cas, R.A.F., Kos, A.M., Hallworth, M., 1999. Gravity currents descending a ramp in a stratified tank. J. Fluid Mech. 379, 39–70. https://doi.org/10.1017/s0022112098003280.

Monaghan, J.J., Kos, A., 1999. Solitary waves on a cretan beach. J. Waterw. Port, Coast. Ocean Eng. 125, 145–154. https://doi.org/10.1061/(ASCE)0733-950X, 1999)125:3 (145.

Monaghan, J.J., Kos, A., Issa, N., 2003. Fluid motion generated by impact. J. Waterw. Port, Coast. Ocean Eng. 129, 250–259.

O'Connor, J., Rogers, B.D., 2021. A fluid-structure interaction model for free-surface flows and flexible structures using smoothed particle hydrodynamics on a GPU. J. Fluid Struct. 104, 103312 https://doi.org/10.1016/j.jfluidstructs.2021.103312.

Ozmen-Cagatay, H., Kocaman, S., 2010. Dam-break flows during initial stage using SWE and RANS approaches. J. Hydraul. Res. 48, 603–611. https://doi.org/10.1080/00221686.2010.507342.

Ozmen-Cagatay, H., Kocaman, S., Guzel, H., 2014. Investigation of dam-break flood waves in a dry channel with a hump. J. Hydro-Environ. Res. 8, 304–315. https://doi.org/10.1016/j.jher.2014.01.005.

Panciroli, R., Abrate, S., Minak, G., Zucchelli, A., 2012. Hydroelasticity in water-entry problems: comparison between experimental and SPH results. Compos. Struct. 94, 532–539. https://doi.org/10.1016/j.compstruct.2011.08.016.

Rafiee, A., Thiagarajan, K.P., 2009. An SPH projection method for simulating fluid-hypoelastic structure interaction. Comput. Methods Appl. Mech. Eng. 198, 2785–2795. https://doi.org/10.1016/j.cma.2009.04.001.

Ropero-Giralda, P., Crespo, A.J.C., Tagliafierro, B., Altomare, C., Domínguez, J.M., Gómez-Gesteira, M., Viccione, G., 2020. Efficiency and survivability analysis of a point-absorber wave energy converter using DualSPHysics. Renew. Energy 162, 1763–1776. https://doi.org/10.1016/j.renene.2020.10.012.

Su, H.J., 2009. A pseudorigid-body 3r model for determining large deflection of cantilever beams subject to tip loads. J. Mech. Robot. 1, 1–9. https://doi.org/10.1115/1.3046148.

Sun, P.N., Le Touzé, D., Oger, G., Zhang, A.M., 2021. An accurate FSI-SPH modeling of challenging fluid-structure interaction problems in two and three dimensions. Ocean Eng. 221 https://doi.org/10.1016/j.oceaneng.2020.108552.

Sun, Z., Zhang, G.Y., Zong, Z., Djidjeli, K., Xing, J.T., 2019. Numerical analysis of violent hydroelastic problems based on a mixed MPS-mode superposition method. Ocean Eng. 179, 285–297. https://doi.org/10.1016/j.oceaneng.2019.03.032.

Tang, Y., Jiang, Q., Zhou, C., 2018. A Lagrangian-based SPH-DEM model for fluid–solid interaction with free surface flow in two dimensions. Appl. Math. Model. 62, 436–460. https://doi.org/10.1016/j.apm.2018.06.013.

Tasora, A., Anitescu, M., 2011. A matrix-free cone complementarity approach for solving large-scale, nonsmooth, rigid body dynamics. Comput. Methods Appl. Mech. Eng. 200, 439–453. https://doi.org/10.1016/j.cma.2010.06.030.

Tasora, A., Serban, R., Mazhar, H., Pazouki, A., Melanz, D., Fleiscmann, J., Taylor, M., Sugiyama, H., Negrut, D., 2016. Chrono: an Open Source Multi-Physics Dynamics Engine. https://doi.org/10.1007/978-3-319-40361-8.

Venkiteswaran, V.K., Su, H.J., 2015. A parameter optimization framework for determining the pseudo-rigid-body model of cantilever-beams. Precis. Eng. 40, 46–54. https://doi.org/10.1016/j.precisioneng.2014.10.002.

Verlet, L., 1967. Computer experiments on classical fluids. I. Thermodynamical properties of Lennard-Jones molecules. Phys. Rev. 159, 98–103. https://doi.org/10.1088/0022-3727/9/2/008.

Wang, H., Qin, Q.-H., 2019. Mechanics of solids and structures. In: Methods of Fundamental Solutions in Solid Mechanics. Elsevier, pp. 53–90. https://doi.org/10.1016/B978-0-12-818283-3.00002-6.

Wei, Z., Edge, B.L., Dalrymple, R.A., Hérault, A., 2019. Modeling of wave energy converters by GPUSPH and Project Chrono. Ocean Eng. 183, 332–349. https://doi.org/10.1016/j.oceaneng.2019.04.029.

Wendland, H., 1995. Piecewise polynomial, positive definite and compactly supported radial functions of minimal degree. Adv. Comput. Math. 4, 389–396.

Wu, K., Yang, D., Wright, N., 2016. A coupled SPH-DEM model for fluid-structure interaction problems with free-surface flow and structural failure. Comput. Struct. 177, 141–161. https://doi.org/10.1016/j.compstruc.2016.08.012.

Xu, X., Jiang, Y.L., Yu, P., 2021. SPH simulations of 3D dam-break flow against various forms of the obstacle: toward an optimal design. Ocean Eng. 229, 108978 https://doi.org/10.1016/j.oceaneng.2021.108978.

Yang, Q., Jones, V., McCue, L., 2012. Free-surface flow interactions with deformable structures using an SPH-FEM model. Ocean Eng. 55, 136–147. https://doi.org/10.1016/j.oceaneng.2012.06.031.

Yang, X., Liu, M., Peng, S., Huang, C., 2016. Numerical modeling of dam-break flow impacting on flexible structures using an improved SPH-EBG method. Coast. Eng. 108, 56–64. https://doi.org/10.1016/j.coastaleng.2015.11.007.

Yilmaz, A., Kocaman, S., Demirci, M., 2021. Numerical modeling of the dam-break wave impact on elastic sluice gate: a new benchmark case for hydroelasticity problems. Ocean Eng. 231, 108870 https://doi.org/10.1016/j.oceaneng.2021.108870.

Yu, Y.Q., Zhu, S.K., 2017. 5R pseudo-rigid-body model for inflection beams in compliant mechanisms. Mech. Mach. Theor. 116, 501–512. https://doi.org/10.1016/j.mechmachtheory.2017.06.016.

Zhan, L., Peng, C., Zhang, B., Wu, W., 2019. A stabilized TL–WC SPH approach with GPU acceleration for three-dimensional fluid–structure interaction. J. Fluid Struct. 86, 329–353. https://doi.org/10.1016/j.jfluidstructs.2019.02.002.